Review on zirconia air-fuel ratio sensors for automotive applications

JONG-HEUN LEE
Division of Materials Science and Engineering, Korea University, Seoul 136-701, Korea
E-mail: jongheun@korea.ac.kr

During the operation of a gasoline engine, the air-fuel ratio (A/F) is a key parameter in controlling fuel consumption and pollutant emissions. In this article, the various zirconia A/F sensors for automotive applications such as the stoichiometric λ sensor, the limiting current-type sensor, and the wide range A/F sensor were reviewed in the viewpoint of the necessity, structure, operation principle, long-term stability, and the algorithm for catalyst monitoring. The miniaturization and simplification of a sensor design using co-firing and planar processing technology will be an effective approach to improve the performance and cost-effectiveness of the sensor. © *2003 Kluwer Academic Publishers*

1. Introduction

The automobile has been the major mode of transportation modality for mankind from the end of 19th century. Because it is powered by the combustion of hydrocarbon fuel, the air-fuel ratio (A/F) during combustion is a key parameter in controlling fuel consumption and pollutant emissions [1–6]. Automotive emissions such as CO, C_mH_n, and NO_x are not only harmful but can also result in acid rain and increase the ground-level ozone concentration. Triggered by the Los Angeles smog in the 1960s in the USA, many advanced countries mandated the 3-way catalytic converter and the zirconia A/F sensor since the 1970s. The 3-way catalyst reduces NO_x into N_2 and oxidizes CO and C_mH_n into CO_2 and H_2O [7–9]. The concentration cell-type zirconia A/F sensor, known as a λ sensor, operates the engine at the stoichiometric point ($A/F \cong 14.7$ for gasoline engine) to obtain the maximum catalytic conversion efficiency.

In gasoline engines, slightly rich (fuel rich), stoichiometric, and lean (fuel lean) conditions are effective in achieving the maximum power, lower pollutant emission, and the maximum fuel economy, respectively. Currently, most gasoline engines are being operated at the stoichiometric point due to environmental concerns [10–12]. Recently, the lean burn and GDI (gasoline direct injection) engines were suggested as an alternative to save fuel consumption because they operated at the lean condition. For this, a wide range A/F sensor that detects the A/F as a proportional signal was developed [13–20]. The limiting current-type sensor is generally employed to obtain a linear signal [21–26]. Regulations for automotive emission are becoming increasingly strict and stringent. A car should detect a malfunction of the automotive parts related to pollutant emission within 1–2 driving cycles. Those are the so-called OBD (On-Board Diagnostics) programs that were first suggested by CARB (California Air Resources Board) and the EPA (U.S. Environmental Protection Agency). One core concept of the OBD is the detection of a deterioration and failure of the 3-way catalyst, which is technically challenging. The A/F before the catalyst fluctuates approximately ± 0.5 near an $A/F = 14.7$, while the variation in the A/F after catalyst decreases to a large extent. Therefore, the signal comparison between the two identical A/F sensors located before and after catalyst can be used to monitor the catalytic conversion efficiency and two λ sensors methods are being used at present [27–31]. This indicates that the A/F sensors are again very important for catalyst monitoring.

In this article, the evolution of the various zirconia A/F sensors, such as the stoichiometric λ sensor, the limiting current-type sensor, and the wide range A/F sensors are reviewed by investigating their necessity, structure, operation principle, and long-term stability, in addition to the algorithm for catalyst monitoring.

2. Concentration cell-type A/F ratio sensor (λ sensor)

2.1. Sensor structure and sensing principle

If lower-valence oxide materials such as CaO, MgO, and Y_2O_3 are added to ZrO_2, the additive cations replace the Zr^{4+} ion, which create a doubly ionized oxygen vacancy to compensate for the charge neutrality. The following shows the incorporation reaction of Y_2O_3 into ZrO_2.

$$Y_2O_3 \xrightarrow{2ZrO_2} 2Y'_{Zr} + 3O_O^X + V_O^{\prime\prime} \qquad (1)$$
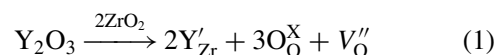
The addition of Y_2O_3 beyond a certain concentration stabilizes the cubic fluorite structure which is a purely oxygen-ion conducting solid electrolyte. The oxygen concentration cell can be established by coating a porous platinum electrode on both sides. The open cell voltage between the electrodes then detects the oxygen
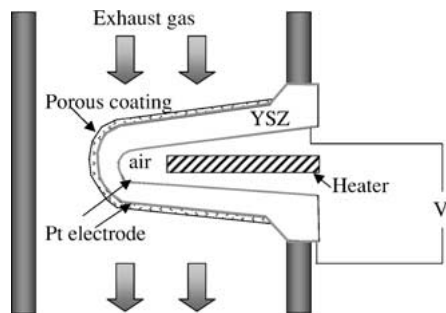
Figure 1 Schematic sensor structure of the concentration cell-type zirconia lambda sensor.

Figure 2 HC, CO, and NO_x emissions after the 3-way catalyst and the λ-sensor signal as a function of A/F.

concentration difference across the electrolyte. Fully stabilized cubic zirconia is generally used to obtain the higher conductivity. Partially stabilized tetragonal zirconia can be also used to increase the thermal-shock resistance and the conductivity at low temperatures [5, 32].

Fig. 1 shows a schematic diagram of the representative stoichiometric sensor for an automobile. It is also known as the λ-sensor, the EGO (Exhaust Gas Oxygen) sensor and the HEGO (Heated Exhaust Gas Oxygen) sensor. As shown in the figure, the inner and outer parts of the thimble-shaped sensor are exposed to an air reference and the automotive exhaust gas, respectively. The electromotive force (EMF) of the cell can be given in the following Nernst equation [10]

$$V = t_{\text{ion}} \frac{RT}{4F} \ln \left(\frac{P_{O_2}(\text{air})}{P_{O_2}} \right) \tag{2}$$

where t_{ion}, R, T, F, P_{O_2} (air), P_{O_2} are the ionic transference number, universal gas constant, absolute temperature, Faraday constant, and the oxygen partial pressures of the air reference and emission, respectively. In equation, '4F' states that 4 electrons are involved in changing an O_2 molecule at the cathode to $2O^{2-}$ and then recovering it to an O_2 molecule at the anode. The EMF shows the maximum value when the electrolyte is a complete ionic conductor ($t_{\text{ion}} = 1$) and decreases when the mixed conduction or electronic conduction dominates. Therefore, pure solid electrolyte is desirable for the sensor application. The oxygen ionization at the triple phase boundary becomes difficult at low temperatures due to insufficient catalytic activity, whereas the oxygen partial pressure regime for the solid electrolytic behavior becomes narrow at high temperature. Therefore, the sensors generally operate between 400–700°C.

The λ sensor is widely used in the stoichiometric control of a gasoline engine [3, 5, 33]. Fig. 2 shows the HC, CO, and NO_x emissions after the catalytic aftertreatment and the EMF profile as a function of the A/F ratio. In the figure, λ means the normalized A/F by the stoichiometric point ($A/F \cong 14.7$ for gasoline). The CO and HC emissions become dominant at the rich condition while NO_x emission increases at the lean condition. Therefore, the maximum efficiency of the catalytic converter can be attained at the stoichiometric point because both of the harmful reducing and oxidiz-
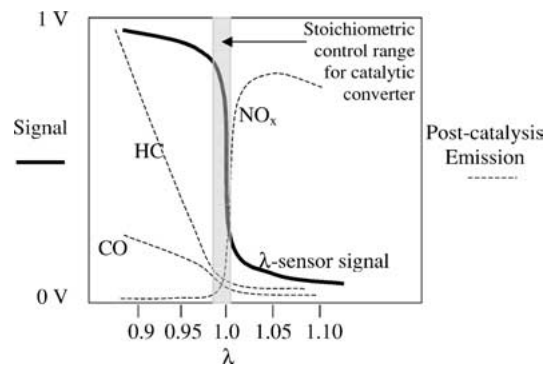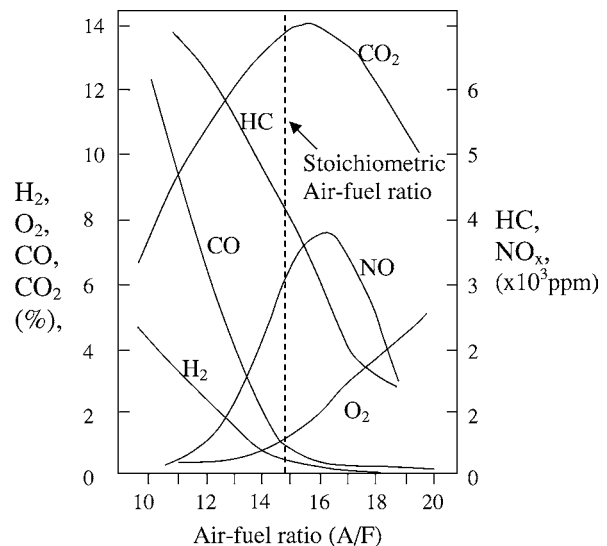

Figure 3 HC, CO, H_2, O_2, and CO emissions before the 3-way catalyst as a function of the A/F ratio, according to [12].

ing gases are oxidized and reduced simultaneously. It is the reason why most gasoline engines operated at the stoichiometric point.

The automotive emissions before catalyst as a function of A/F are given in Fig. 3 [12]. The trace CO and H_2 can be found even at the lean condition and trace amounts of O_2 are emitted even at the rich condition. This is possible because the automotive emissions are not in chemical equilibrium. The non-equilibrium state becomes increasingly important when the air and fuel intake mixture is heterogeneous [34]. Therefore, detecting the free O_2 concentration in the emission will not reflect the accurate A/F ratio during combustion. This means that the equilibrium O_2 concentration after the sufficient reaction with C_mH_n and CO is a precise measure of the A/F ratio. Porous platinum plays a role as a catalyst to promote equilibration between the gases [35]. In Fig. 2, the sensor EMF decreases rapidly at $\lambda = 1$, which is because the equilibrium O_2 concentration increases abruptly from the rich (typical $P_{O_2} = 10^{-20}$) to the lean (typical $P_{O_2} = 10^{-3}$) state near the stoichiometric point.

Fig. 4 shows a schematic diagram how the λ sensor operates the engine at the stoichiometric point. From the signal of the air flow sensor, the engine can be operated
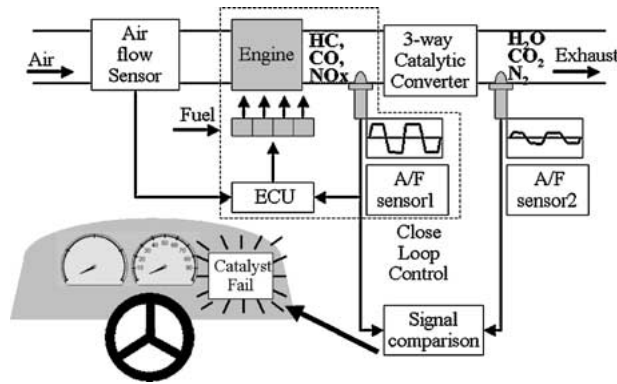
Figure 4 The A schematic diagram of the 'Close Loop Control' using a concentration cell-type zirconia λ sensor and catalyst monitoring by comparing the signals of two A/F sensors located before and after the 3-way catalyst.

Figure 6 The schematic mechanism of lean shift, according to [38].

approximately at the stoichiometric point. However, accurate control at the stoichiometric point merely by the air flow sensor is almost impossible due to the inevitable error in the air flow sensor and the compositional variations in gasoline. Therefore, the precise stoichiometric point is determined from the emission, which is directly correlated to the A/F ratio. If the λ sensor sent the signal to ECU (engine control unit), the ECU reduces or increases the amount of fuel injected to maintain the stoichiometric point. This is known as the 'Feedback control' or the 'Close Loop Control' [36, 37].

2.2. Lean shift

The largest hurdle in measuring the stoichiometric point using a λ sensor is the 'lean shift'. Schematic diagrams of lean shift are shown in Figs 5 and 6. As shown in Fig. 5, the 'lean shift' means that the EMF profile of the sensor as a function of the A/F ratio shifts to the lean region. Therefore, the lean-shifted sensor determines the stoichiometric point as being 'fuel rich', which operates the engine at the slightly lean region.

The lean shift emanates from the limited gas diffusion across the porous coating shown in Fig. 1, which is used to protect the catalytic activity of the outer electrode from poisoning elements in the emission [35, 38]. Saji *et al.* [38] measured the EMF of the λ sensor with a porous coating using various reducing gases such as H_2, D_2, CO, CH_4, and i-C_4H_{10} with the supporting gases such as N_2-O_2. They reported that the smaller molecular weight of the reducing gas resulted in a larger lean shift
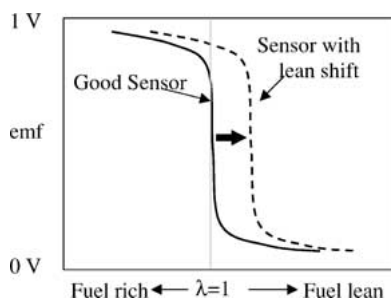

Figure 5 The EMF profiles of a good lambda sensor and a lean-shifted sensor.
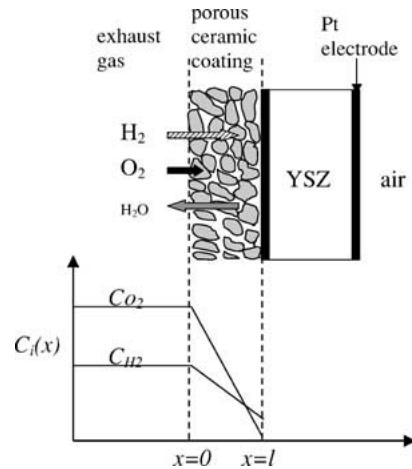
and that i-C_4H_{10} being heavier than O_2 and N_2 showed a 'rich shift'. This explains that the gas concentrations near the electrode become different from those outside the porous layer as a result of the different gas diffusion rates.

This can be explained as follows: In order to simplify a complex gas composition, let us assume a stoichiometric H_2-O_2-N_2 mixture ($C_{H_2}(0):C_{O_2}(0) = 2:1$). The H_2 and O_2 flux (J_{H_2} and J_{O_2}) when the gases diffuse through the porous ceramic coating can be calculated by the following equation:

$$J_{H_2} = -\frac{D^*_{H_2}}{l}\big[C_{H_2}(0) - C_{H_2}(l)\big] \qquad (3)$$

$$J_{O_2} = -\frac{D^*_{O_2}}{l}\big[C_{O_2}(0) - C_{O_2}(l)\big] \qquad (4)$$

where $C_i(0)$, $C_i(l)$, l, $D^*_{H_2}$, and $D^*_{O_2}$ are the concentrations of the i gases at the top and bottom of the protective coating, the thickness of the protective coating, the gas diffusion coefficients of H_2 and O_2, respectively. Assuming steady state and a sufficient catalytic efficiency of the Pt electrode, J_{H_2} should be $2J_{O_2}$ because two H_2 molecules are oxidized into H_2O vapor by a reaction with an O_2 molecule. The following equation can be attained if $C_{H_2}(0):C_{O_2}(0) = 2:1$ and $J_{H_2} = 2J_{O_2}$ are combined with Equations 3 and 4 as follows:

$$K'\left[1 - \frac{C_{H_2}(l)}{2C_{O_2}(0)}\right] = \left[1 - \frac{C_{O_2}(l)}{C_{O_2}(0)}\right] \qquad (5)$$

$$K' = \frac{D^*_{H_2}}{D^*_{O_2}} \qquad (6)$$

In Equation 6, $D^*_{H_2}$ is equal to $4D^*_{O_2}$ in a pure gas form because the gas diffusion coefficient is inversely proportional to the square root of the molecular weight. Furthermore, even if one considers the supporting gases such as N_2 and O_2, $D^*_{H_2}$ should be larger than $D^*_{O_2}$. The $K' > 1$ in Equation 5 means $C_{H_2}(l)/2C_{O_2}(0) > C_{O_2}(l)/C_{O_2}(0)$. This again says that $C_{H_2}(l) > 2C_{O_2}(l)$, i.e., the gas near the electrode becomes rich even at the stoichiometric composition outside the porous coating.

CHEMICAL SENSORS

The real situation is even more complex than the aforementioned case. The amount of the lean shift will be determined by competition between the lean shift by H_2 and CO and the rich shift by C_mH_n ($m \geq 2$). Generally speaking, the deposition of particulate matter on the porous coating causes a gradual lean shift as the sensor ages. It should be noted that the above discussion assumes identical gas adsorption to the Pt electrode and the sufficient catalytic effect of Pt. Therefore, other factors such as gas adsorption and catalytic effect should be taken into account in order to comprehend an anomalous EMF behavior when the aforementioned assumption becomes invalid [39].

2.3. Small plate-type λ sensor

At the cold start of engine, a thimble-shape λ sensor without a heater should wait at least 3 min for the proper operation because heating the zirconia solid electrolyte to the minimum operation temperature (approximately 400°C) relies totally upon the hot automotive emissions. The installation of a heater in the A/F sensor enables a faster warm-up and a higher operation temperature of the sensor [40, 41]. Generally speaking, approximately 50% of the harmful HC emission during 1 h driving comes from the initial 2 min after a cold start. This is mainly due to the slow warm-up of the 3-way catalyst and the λ sensor. Therefore, shortening the sensor warm-up time to approximately 30 sec by employing a heater will significantly reduce pollutant emission. To maximize the quick warm-up characteristics, a small plate-type λ sensor fabricated by ceramic tape casting technology has been suggested [5, 42]. The core idea is to reduce the thermal mass of the sensor with an identical heater power. The thimble-shape λ sensors are approximately 1 cm wide in diameter and 5 cm long. However, the co-firing of the laminate between the green sheets decreases the sensor thickness to 2–3 mm, which shortens the warm-up time to approximately 10 sec. This type of sensor has been developed or is under the development by several sensor makers.

2.4. Small plate-type λ sensors with a pseudo oxygen reference

The aforementioned λ sensors require an air reference to measure the EMF. However, the fabrication of an air reference results in many technical difficulties, which includes the materials processing of a sensor element and the gas tight sealing in the sensor housing. Furthermore, the sensor housings at the side of air reference should be waterproof while sufficient air should be provided to the reference electrode. This makes the sensor structure complex. In order to simplify the sensor element and housing, a λ sensor using a pseudo oxygen reference has been suggested [43, 44], and the schematic sensor structure is illustrated in Fig. 7. The important idea is the serial connection of a resistance to the sensor. When 14 V DC is applied to a cold sensor, the most potential drops across the zirconia sensor because it is dielectric at low temperatures. After heating the sensor
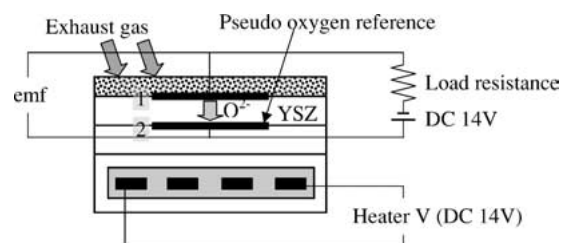

Figure 7 The structure of a small plate-type λ sensor with a pseudo oxygen reference.

element, the cell resistance (R_b) becomes much smaller than the series resistance. Although the R_b value in the rich condition is approximately 2 times larger than that in the lean region, the current across the cell becomes approximately the same because the series resistance is much larger than the R_b values. The O_2 will accumulate at electrode 2 by O_2 pumping from electrode 1. Approximately the same P_{O_2} can be attained at electrode 2 due to the low outward leakage of O_2 when the laminated zirconia layers are dense. Moreover, even if there is a small P_{O_2} difference (in electrode 2) between the fuel rich and lean conditions, this variation would be negligible compared to a large P_{O_2} variation from 10^{-3} to 10^{-20}. The EMF of this sensor can be explained by the following equation

$$V = I_P R_b + \frac{RT}{4F} \ln \left(\frac{P_{O_2}(\text{ref})}{P_{O_2}(\text{exh.})} \right) \qquad (7)$$

where P_{O_2} (ref) and P_{O_2} (exh.) are P_{O_2} at the pseudo oxygen reference and exhaust sides, respectively. In the sensor operation, the left $I_p R_b$ term can be set to a negligibly small number compared to the right Nernst EMF term by the proper combination of I_p and R_b [45, 46]. This means that the λ sensor with a pseudo oxygen reference shows an EMF behavior almost identical to that of a conventional λ sensor. The main advantages of this sensor are the simple fabrication of the sensor element and housing.

2.5. The long-term stability of sensor

The main issues in the long-term stability of a sensor are as follows: (1) The total length of the triple phase boundary decreases significantly as a result of grain growth of the Pt particles when the sensor is exposed to high temperatures for an extended time, which slows the response time. (2) H_2S, SO_2 and Pb contained within the emission are known to poison the catalytic activity [47, 48]. The porous coating in Fig. 1 is used to protect the catalytic activity of the electrode [39, 49, 50]. Therefore, the porous coating in the λ sensor should be designed to be sufficiently dense to protect the poisoning element and be properly porous in order to prevent the lean shift phenomenon.

3. Limiting current-type sensor
3.1. Relationship between the limiting current and the gas-diffusion mechanism

When a dc electric field is applied to a Pt|YSZ|Pt cell, O_2 at the cathode side is pumped to the anode side by
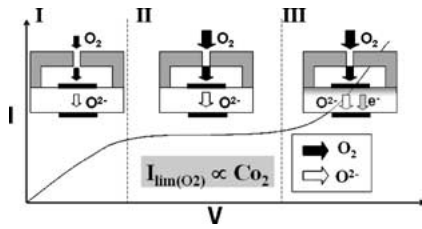
at the stationary state can be given in the following equation [51]

$$J_{O_2} = -D_{O_{2,N}}\frac{dC_{O_2}}{dz} + X_{O_2}J_{O_2} \qquad (11)$$

where $D_{O_{2,N}}$, C_{O_2}, and X_{O_2} are the normal diffusion coefficient (m²/s), the molar concentration (mol/m³), and the molar fraction of O_2, respectively. When assuming O_2 as an ideal gas, the C_{O_2} can be represented by

$$C_{O_2} = \frac{N_{O_2}}{V} = \frac{P_{O_2}}{RT} = \frac{X_{O_2}P}{RT} \qquad (12)$$

where N_{O_2} (mol), V (m³), and P (kg/m·s²) are the molar number of O_2, volume, and total pressure, respectively. The boundary conditions can be given at the top and bottom of the pores with a length of l

$$z = 0 \quad C_{O_2} = C_{O_2} \text{ (ambient)} \qquad (13)$$
$$z = l \quad C_{O_2} = C_{O_2}(h) \ll C_{O_2} \text{ (ambient)} \quad (14)$$

where $C_{O_2}(h)$ is the O_2 concentration near the cathode. The solution of the differential Equation 11 using Equation 12 and the boundary conditions, 13 and 14 is shown in the following equation:

$$J_{O_2} = -\frac{D_{O_{2,N}}P}{RTl}\ln\left[1 - X_{O_2}\text{ (ambient)}\right] \qquad (15)$$

The limiting current ($I_{\text{lim,N}}$) is determined by J_{O_2} and the cross-sectional area of the pore (S).

$$I_{\text{lim,N}} = 4FSJ_{O_2}$$
$$= -\frac{4FD_{O_{2,N}}SP}{RTl}\ln\left[1 - X_{O_2}\text{ (ambient)}\right] \quad (16)$$

The equation shows that the limiting current according to the normal diffusion is proportional to $-\ln(1 - X_{O_{2(\text{ambient})}})$. The normal diffusion coefficient (D_N) shows the following dependence upon T and P [51]

$$D_N = D_S\left(\frac{T}{273}\right)^a\frac{1}{P} \qquad (17)$$

where D_s is the standard diffusion coefficient at 273 K and 1 atm and α is constant depending on the type and composition of a gas. From a combination of Equations 16 and 17, it can be seen that $I_{\text{lim,N}}$ is proportional to $T^{\alpha-1}$ and is independent of P. According to Usui et al. [51], the $\alpha - 1$ value ranged from 0.66 to 0.75 when He, Ne, Ar, and N_2 gases were the supporting gases. Therefore, the $\alpha - 1$ value can be considered to be approximately 0.75 in normal diffusion.

Under Knudsen diffusion, the collision between O_2 molecules and the pore becomes more dominant than the collision between O_2 molecules. Therefore, the oxygen diffusion becomes independent upon the pressure gradient across the pore, and the oxygen flux can be given as follows [51]:

$$J_{O_2} = -D_{O_{2,K}}\frac{dC_{O_2}}{dz} \qquad (18)$$

Figure 8 The characteristic of limiting current with regard to O_2 in an oxidizing atmosphere.

the following reaction.

$$O_2 + 4e^- \rightarrow 2O^{2-} \qquad \text{(cathode)} \qquad (8)$$
$$2O^{2-} \rightarrow O_2 + 4e^- \qquad \text{(anode)} \qquad (9)$$

If a gas diffusion barrier is attached to the cathode side of a O_2 pumping cell, a limiting current can be observed, as schematically shown in Fig. 8 [21]. When the amount of O_2 pumped is smaller than the diffuse-in amount of O_2, the O_2 pumping current (I_p) increases linearly according to the applied voltage (region I). However, the inward diffusion of O_2 across the diffusion barrier becomes the rate determining step in O_2 pumping at high V. Therefore, the I_p value remains constant despite the increase in voltage (region II). The limiting current refers the current plateau due to limited gas diffusion. The amount of gas diffusion is proportional to O_2 concentration gradient according to Fick's first law, and the O_2 concentration near the cathode in the limiting current regime is negligibly small. Therefore, the limiting current is linear near the atmospheric O_2 concentration [22–24]. Compared to the concentration cell-type zirconia sensor, the limiting current-type sensor has advantages in providing a more precise and linear detection of a higher O_2 concentration.

The current increase in region III can be attributed to the electronic conduction due to the decomposition of ZrO_2 in low P_{O_2}. According to a report, the P_{O_2} for ZrO_2 decomposition is $<10^{-36}$ at 700°C [21] and the reaction can be given as follows:

$$O_O = V_O^{\cdot\cdot} + \frac{1}{2}O_2 + 2e^- \qquad (10)$$
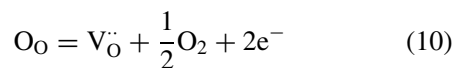
The normal and Knudsen mechanisms can be considered in the diffusion of O_2 through the pores in the limiting current-type sensor. When the pore sizes are much larger than the mean free path of a gas molecule, normal diffusion occurs and gas diffusion depends primarily on collisions between the gas molecules. On the other hand, Knudsen diffusion occurs when the pore diameter is comparable or smaller than the mean free path. The collision between the gas molecule and the outer walls of the pores becomes dominant in the diffusion. The dependence of the limiting current upon temperature, pressure, and the oxygen concentration is known to critically correlate to the type of gas diffusion. Therefore, the pore size in the limiting current should be designed according to the operation environment of the sensor.

In normal diffusion, O_2 diffuses by an O_2 concentration gradient and a pressure gradient across the pore. Therefore, one-dimensional oxygen flux through a pore

where $D_{O_2,K}$ is the Knudsen diffusion coefficient of O_2. The limiting current according to the Knudsen diffusion ($I_{lim,K}$) can be given in the following equation by solving Equation 18 using the same boundary conditions.

$$I_{lim,K} = \frac{4FD_{O_2,K}SP}{RTl} X_{O_2} \text{ (ambient)} \qquad (19)$$

where $D_{O_2,K}$ is the Knudsen diffusion coefficient of O_2. The Knudsen diffusion coefficient of i gas ($D_{K,i}$) is given as follows [52, 53]

$$D_{K,i} = \frac{2}{3}d\sqrt{\frac{2RT}{\pi M_i}} \qquad (20)$$

where d and M_i are the diameter of pore and molecular weight of the diffusing gas i. In this equation, it can be seen that the Knudsen diffusion coefficient of a pure gas is inversely proportional to the square root of the molecular weight. However, in a real situation, there are supporting gases besides the diffusing species. Therefore, the Knudsen diffusion coefficient varies according to the species and the amount of supporting gas. Qualitatively speaking, the smaller diffusion coefficient can be expected in the heavier supporting gases [54, 55]. The following equation can be attained by applying Equation 20 to Equation 19

$$I_{lim,K} = \frac{4FSP}{RTl}\frac{2}{3}d\sqrt{\frac{2RT}{\pi M_i}}X_{O_2} = \frac{4FSP}{RTl}K\sqrt{\frac{T}{M_i}}X_{O_2} \qquad (21)$$

where K is a constant ($kg^{1/2}$ m/s $K^{1/2}$) which is independent of T and P. Hereafter, the X_{O_2} (ambient) will be denoted as X_{O_2} for simplicity. In above equation, the limiting current according to Knudsen diffusion is proportional to $T^{-0.5}$ and P. Table I summarizes the limiting-current characteristics by normal and Knudsen diffusion. Normal diffusion, Knudsen diffusion, and mixed diffusion are desirable in eliminating the P dependence, for linear sensing, and in minimizing the T dependence, respectively. This clearly shows that pore size control is a key parameter in manipulating the signal dependence upon T, P, and X_{O_2}.

3.2. The limiting current in O_2-CO_2-N_2 and CO-CO_2-N_2 atmospheres

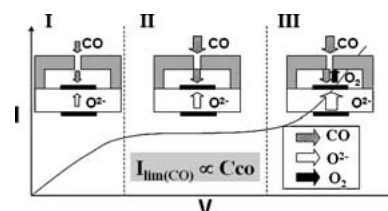The following equation describes the I-V characteristics of the limiting current-type sensor when a dc

Figure 9 The characteristic of limiting current with regard to CO in a reducing atmosphere.

voltage (V) is applied.

$$V = I_p R_b + \frac{RT}{4F}\ln\left(\frac{X_{O_2}}{X_{O_2(h)}}\right) \qquad (22)$$

where X_{O_2} and $X_{O_2}(h)$ are the molar fractions of O_2 at the atmosphere and inside the cavity. The equation states that the O_2 pumping current (I_p) is determined by the resistance of the O_2 pumping cell (R_b) and the O_2 concentration gradient across the gas diffusion barrier. The limiting current with regard to O_2 is approximately constant within the limiting current region. This implies that a voltage increment (ΔV) in the current plateau is compensated by an exponential decrease in $X_{O_2}(h)$.

The limiting current with regard to reducing gases such as H_2, CO, and C_mH_n can be also attained when O_2 is pumped into the gas diffusion barrier [56, 57]. Fig. 9 illustrates the schematic sensing mechanism. When O_2 is pumped into the cavity, the pumped O_2 oxidizes CO into CO_2. Because the applied voltage and the direction of O_2 pumping are reversed, the signs of V and I_p are negative. In region I, the EMF due to the concentration gradient is negligible compared to the $I_p R_b$ term. Therefore, $-I_p$ linearly increases with $-V$. In region II, the limiting current with regard to CO can be attained because the oxidative consumption of CO gas depends on the diffuse-in amount of CO gas. In Equation 22, the approximately constant current (I_p) means that the increment in $-V$ is compensated by the increase in $X_{O_2}(h)$.

As explained, a limiting current can be attained not only in oxidizing gases such as O_2 and but also in reducing gases such as CO, H_2, and C_mH_n. The limiting current is the principal algorithm in measuring the A/F. The automotive emission consists of CO, H_2, and C_mH_n, CO_2, H_2O, N_2, O_2, and NO_x. CO, H_2, and C_mH_n emissions are dominant in the rich condition while O_2 emitted to a large extent in the lean condition. In both conditions, both CO_2 and H_2O are abundant. Therefore, the concentrations of the oxidizing or reducing gases

TABLE I Limiting current characteristics at the normal diffusion and Knudsen diffusion

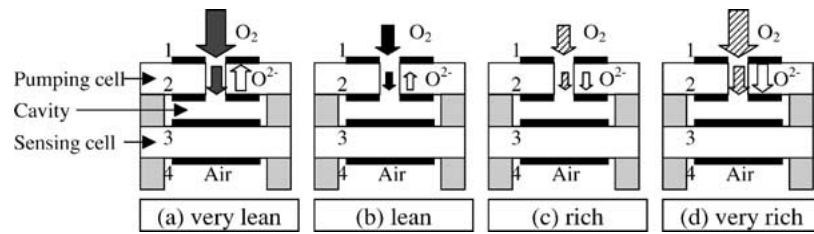|	Normal diffusion	Knudsen diffusion
Pore diameter (d)	$d \gg$ mean free path	$d <$ mean free path
Limiting current	$I_{lim,N} = -\frac{4FD_{O_2,N}SP}{RTl}\ln(1 - X_{O_2})$	$I_{lim,K} = \frac{4FD_{O_2,K}SP}{RTl}X_{O_2}$
X_{O_2}	$\propto -\ln(1 - X_{O_2})$	$\propto X_{O_2}$
Pressure (P)	independent upon P	$\propto P$
Temperature (T)	$\propto T^{0.75}$	$\propto T^{-0.5}$
Comment on diffusion barrier	Generally one-hole type	Generally porous layer type

Figure 10 The sensing principle of a wide range air-fuel ratio sensor.

in the supporting gases such as CO_2, H_2O, and N_2 can provide the quantitative information on the A/F ratio. The detailed procedures of calculating the limiting currents with regard to O_2 and CO under the O_2-CO_2-N_2 and CO-CO_2-N_2 atmospheres were shown elsewhere with the experimental result [57].

4. Wide range air-fuel ratio sensor
4.1. Operation principle

Controlling the A/F ratio in the fuel lean region using the λ sensor is difficult because the signal variations in rich or lean regions are very small. In comparison, a wide range A/F sensor detects the limiting current linear to the degree of the fuel rich and fuel lean region.

Fig. 10 shows the operating principle of the wide range A/F ratio sensor. The sensor consists of a limiting current-type sensor and a sensing cell. The O_2 pumping current, which is adjusted to set the EMF of the cell to $\sim$450 mV becomes the sensor signal [16–19]. This means that the P_{O_2} (cavity) is kept at $\sim 10^{-10}$ during the sensor operation. In the fuel lean region ((a), (b)), O_2 should be pumped out to reduce the P_{O_2} (cavity) because the P_{O_2} (exh.) is $\sim 10^{-3}$. More O_2 pumping is necessary to achieve P_{O_2} (cavity) $= 10^{-10}$ at the leaner condition because the oxygen content is higher in the leaner emission. On the other hand, in the rich condition, the equilibrium P_{O_2} in the emission ranges from 10^{-18} to 10^{-20}. This means that O_2 should be pumped into the cavity in order to achieve a P_{O_2} (cavity) $= 10^{-10}$. The richer condition will require more O_2 pumping in the reverse direction. Therefore, if the O_2 pumping direction in the lean condition is defined as positive, the linear current increase with increasing A/F ratio (from (d) to (a)) can be a precise measure of A/F. The polarity of the pumping current will indicate whether the emission is lean or rich.

Fig. 11 shows the typical sensing characteristics of a wide range A/F sensor [58]. The slope in the rich region is larger than that in the lean region. This means that H_2 and CO diffusion in the rich condition is higher than that of O_2 in the lean region. This is because the diffusion coefficient of a lighter gas is larger than that of a heavier gas.

4.2. Wide range air-fuel ratio sensor with a simple gas diffusion barrier

Tanaka *et al.* [59] reported that a wide range of the A/F ratio could be measured simply by coating a gas diffusion barrier on a thimble-shaped λ sensor. Fig. 12 shows the schematic sensing mechanism. An external dc field
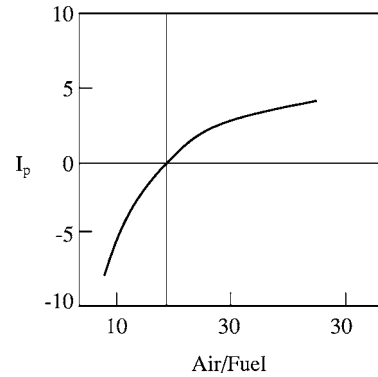

Figure 11 Typical sensing characteristics of a wide range air-fuel ratio sensor, according to [58].

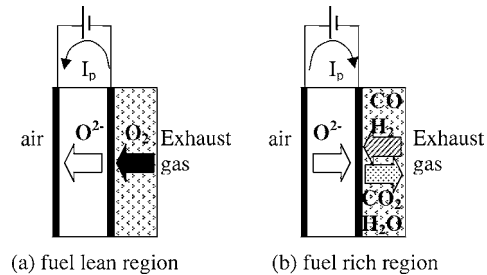*Figure 12* Sensing mechanism of a wide range air-fuel ratio sensor with a simple gas diffusion barrier, according to [59].

was applied against the O_2 concentration gradient during the sensor operation. In the fuel lean region, O_2 was pumped to the air reference side because the O_2 concentration gradient was small compared to the electric field. The O_2 pumping current increased at the leaner condition because more O_2 could diffuse toward electrode 2 (Fig. 12a). In contrast, in the fuel rich region, the EMF from O_2 concentration gradient is larger than the applied voltage. Therefore, O_2 will be pumped from the air to the exhaust side despite the opposite electric field. In this case, the richer condition will pump more O_2 into the exhaust side because a larger concentration gradient will be established between the two electrodes. Therefore, one can obtain the current signal, which is proportional to the degree of fuel rich and fuel lean.

Generally, a wide range A/F sensor needs circuits for the signal comparison and feedback to adjust the pumping current. In comparison, this sensor does not need to change the O_2 pumping direction and the circuit for feedback control. However, the wide area of the gas diffusion barrier can be degraded by repeated thermal shock. Kim *et al*., proposed a small plate-type sensor with a similar sensing algorithm to improve the sensor

warm-up characteristics and to attain a high operation temperature [60].

4.3. UEGO (universal air-fuel ratio heated exhaust gas oxygen) sensor

The UEGO sensor was developed by Yamada *et al.* in the NGK spark plug co. and is being used in lean burn engines [58]. Fig. 13 shows the schematic sensor structure. A pseudo oxygen reference is established at electrode 4 by applying a small current (I_{cp}) to the sensing cell. Note that the sensing cell between electrodes 3 and 4 is similar to the small plate-type λ sensors with a pseudo oxygen reference that was mentioned in Section 2.4. Using the circuits containing a comparator and an integrator, the current of the pumping cell is adjusted to keep the P_{O_2} (cavity) to 10^{-10} (EMF between 3 and 4 is $\sim$450 mV) because it corresponds to the limiting current region for the entire range of the A/F ratio. The catalytic effect of the Pt electrode in this sensor is smaller than in a conventional λ sensor because the sensor was fabricated by co-firing the laminate of the ceramic green sheets at the elevated temperature ($\sim$1500°C). Therefore, it is needed to be operated at a relatively high temperature (600–800°C).

4.4. Planar-type air-fuel ratio sensor

Oh [61] designed a planar-type A/F sensor. As shown in Fig. 14, a porous YSZ layer is coated on a ceramic substrate and two cells were fabricated using a single porous YSZ electrolyte. A pseudo oxygen reference is established by pumping O_2 from electrodes 1 to 2. Then
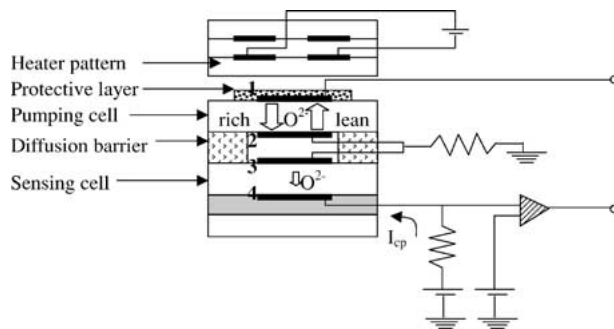

Figure 13 The structure and sensing principle of a UEGO (Universal Air-Fuel Ratio Heated Exhaust Gas Oxygen) sensor, according to [58].
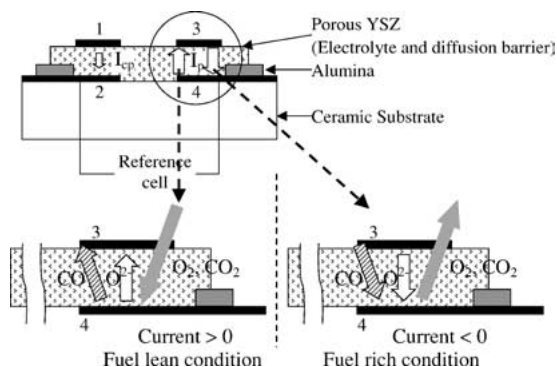

Figure 14 The structure and sensing principle of a planar-type air-fuel ratio sensor, according to [61].
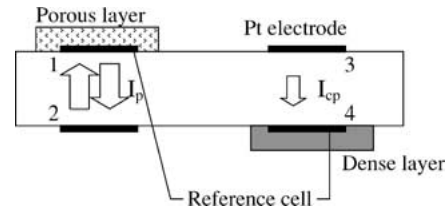

Figure 15 The structure and sensing principle of a plate-type air-fuel ratio sensor, according to [62].

the A/F ratio can be measured from the O_2 pumping current between 3 and 4, which is adjusted to keep a constant EMF between 2 and 4. In order to operate this sensor, P_{O_2} at electrode 4 (P_{O_2} (4)) should be kept at $\sim$10^{-10}, which is similar to keeping P_{O_2} (cavity) in the UEGO sensor. In the fuel lean region, O_2 is pumped from 4 to 3 in order to decrease P_{O_2} (4). The O_2 diffuses from 3 to 4 because the electrolyte is porous. This results in a limiting current with regard to O_2 (Current > 0). In the fuel rich region, the atmospheric P_{O_2} is lower than 10^{-10}. Therefore, O_2 is pumped from 3 to 4 and the O_2 pumping current is limited by the oxidative consumption of the reducing gases at electrode 4. (Current < 0) The application of porous YSZ both as an electrolyte and as a gas diffusion barrier simplifies the sensor structure to a large extent. Furthermore, the fabrication of the A/F sensor in a small size would be advantageous.

4.5. Plate-type air-fuel ratio sensor

Kim and the present author [62] suggested a plate-type A/F sensor using a single YSZ plate. The sensor structure is given in Fig. 15. A pseudo oxygen reference is established by pumping O_2 from electrode 3 to electrode 4, which is covered with a dense layer. The O_2 pumping cell between 2 and 1 with a porous gas diffusion barrier plays the role of the limiting current-type sensor, and the cell between 1 and 4 corresponds to the sensing cell. Therefore, the A/F ratio can be measured if the O_2 pumping current is adjusted to keep P_{O_2} (1) to 10^{-10} using the EMF between 1 and 4. This sensor utilizes a dense YSZ layer, which is advantageous in the light of the mechanical strength a the sensor element. However, small ionic cross talk was observed because the O_2 pumping cell (between 1 and 2) and the sensing cell (between 1 and 4) share one electrode and one electrolyte. Kim *et al.* suggested an algorithm for the sensor operation to exclude the ionic cross-talk phenomenon. The main advantages of the sensor are the simple sensor structure and the potential to be applied to mass production using ceramic tape casting technology.

5. Catalyst monitoring sensor

California firstly mandated an OBD I (On-board diagnostics) system in automobiles. It is a program to monitor all the electronic components that can affect the emissions and to notify the driver of a malfunction of any parts. The important parts for monitoring include the 3-way catalyst and the oxygen sensor. In the view of catalyst monitoring, the detection of catalyst failure is a primary concern in OBD I. Since the OBD II

	Lambda Sensor	Wide range A/F sensor	Simple amperometric sensor suggested by present author
Sensor Characteristics Before catalyst After catalyst	A/F=14.7	A/F=14.7	A/F=14.7
Sensor signal at CE=60%			
Sensing range Principle structure cost	70-100% potentiometric moderate low cost	40-100% amperometric complex high cost	40-100% amperometric simple low cost

Figure 16 The structures, sensing principles and sensing characteristics of various catalyst monitoring sensors.

program was introduced, not only has detecting failure becoming increasingly important, but also the monitoring of catalyst degradation in a quantitative manner is needed. The European Union also began to monitor the catalyst by the EURO III program in 2000. The A/F ratio before the catalyst fluctuates $\sim\pm0.5$ near an A/F of 14.7, while a variation in A/F ratio after the catalyst decreases significantly. The main algorithm of the catalyst degradation using A/F sensors is to compare the signals of two identical sensors located before and after the catalyst [27]. For example, the sensor signals before and after the catalyst becomes almost identical when the catalyst fails.

The λ sensor, the UEGO sensor, and other A/F sensors can be applied to monitor the catalyst. Fig. 16 summarizes the catalyst-monitoring algorithm, the sensor signals before and after the catalyst, the sensor structure, and the monitoring range of the λ sensor, the UEGO sensor, and the simple amperometric sensor proposed by the present author *et al*. [63–65] The λ sensor is cost-effective and the sensor stability was confirmed in the automotive market. However, the sensor signal changes quite abruptly near the stoichiometric point and is almost constant both in the fuel lean and rich regions. Therefore, this method can misjudge a weakly degraded catalyst as a failure. Generally, the two λ sensors method is known to detect a 70–100% catalytic converting efficiency. The UEGO sensor can detect a wider range of catalytic converting effects (approximately 40–100%). Then main reason for the superior sensing is that the limiting current linear to the A/F ratio can detect small changes in the A/F ratio. However, fabricating a stable low-cost sensor remains a challenge.

Present author *et al*. [63–65] proposed a new catalyst monitoring sensors using the limiting current principle with a simple structure and circuit. Fig. 17 shows the structure and operating mechanism of the catalyst monitoring sensor using porous YSZ-Al$_2$O$_3$ composites, which can be used dually as a solid electrolyte and a gas diffusion barrier [64, 65]. The three identical
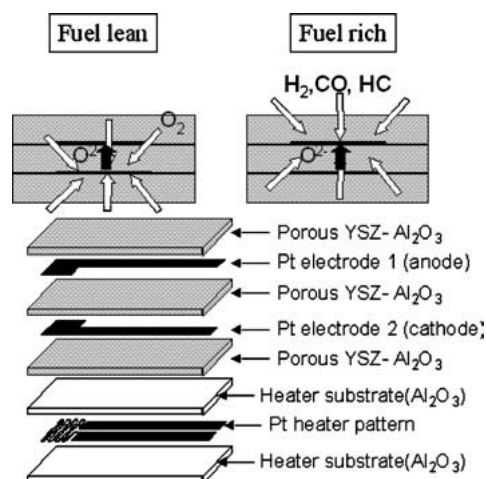

Figure 17 The structure and sensing principle of a catalyst monitoring sensor using porous YSZ-Al$_2$O$_3$ composites dually used as a solid electrolyte and gas diffusion barrier, according to [65].

YSZ-Al$_2$O$_3$ porous layers are stacked and two Pt electrodes are inserted in between. In the lean condition, when O$_2$ is pumped from electrode 2 to electrode 1, O$_2$ diffuses toward electrode 2 through all the three porous YSZ-Al$_2$O$_3$ layers as shown in the arrows because the layers have the same microstructure. In the fuel rich region, the O$_2$ pumped to electrode 1 is consumed by the oxidative reaction with the reducing gases. Therefore, O$_2$ pumping is limited by the diffusion of the reducing gases toward electrode 1. Unlike the UEGO sensor, this sensor does not need to control the direction and amount of O$_2$ pumping, which reduces the driving circuit to a great extent. Furthermore, because all the laminated layers are identical, no shrinkage mismatches between the layers occur during co-firing and an improved resistance to thermal shock is expected. These qualities are promising in terms of fabrication and long-term stability. This study also suggested a limiting current-type sensor and a wide range A/F sensor using porous YSZ-Al$_2$O$_3$ dually as the solid electrolyte and gas diffusion barrier [66, 67].

6. Concluding remarks and the future direction in the air-fuel ratio sensors

Zirconia A/F sensors have been and will be a principal solution to reduce harmful emissions and to improve fuel consumption in automobiles. The λ sensor used to detect the stoichiometric A/F ratio will become smaller in size in order to shorten the sensor warm-up time, which will reduce the emissions concentrated in the initial stages of driving. A small plate-type λ sensor with or without an oxygen reference will be promising in the near future. The wide range A/F sensor has huge potential because more lean-burn and GDI engines to reduce the global warming gas are expected in the near future. The successful mass production of a wide range A/F sensor with a low cost can replace the λ sensor because the linear sensing of the A/F ratio is more convenient to trace the stoichiometric point. Finally, the limiting current principle is desirable for monitoring the catalytic converting efficiency in a quantitative way when the signal comparison between the two A/F sensors is employed.

Acknowledgements

References

1. T. TAKEUCHI, *Sensors and Actuators* **14** (1988) 109.
2. E. C. SUBBARAO and H. S. MAITI, in "Advances in Ceramics," Vol. 24B, edited by S. Somiya, N. Yamamoto and H. Yanagina (The American Ceramic Society, Inc., Westerville, Ohio, 1988) p. 731.
3. E. M. LOGOTHESIS, in "Chemical Sensor Technology," Vol. 3, edited by N. Yamazoe (Kodansa and Elsevier, 1991) p. 89.
4. M. BENAMMAR, *Meas. Sci. Technol.* **5** (1994) 757.
5. J. RIEGEL, H. NEUMANN and H.-M. WIEDENMANN, *Solid State Ionics* **152–153** (2002) 783.
6. W. C. MASKELL, *ibid.* **134** (2000) 43.
7. H. C. YAO and Y. F. Y. YAO, *J. Catalyst.* **86** (1984) 254.
8. G. B. FISHER, J. R. THESIS, M. V. CASARELLA and S. T. MAHAN, SAE Paper No. 931034, 1993.
9. J. R. THEIS, W. J. LABARGE and G. B. FISHER, SAE Paper No. 932666, 1993.
10. C. M. MARI and G. B. BARBI, in "Chemical Sensor Technology," Vol. 4, editied by S. Yamauchi, Chemical Sensor Technology (Kodansa Ltd. and Elsevier, 1992) p. 99.
11. E. HAMANN, H. MANGER and L. STEINKE, SAE paper No. 770401, 1977.
12. P. MCGEEHIN, *J. Br. Ceram. Soc.* **80** (1981) 37.
13. E. IVERSE-TIFFÉE, K. H. HÄRDTLE, W. MANESKLOU and J. RIEGEL, *Electrochimca Acta* **47** (2001) 807.
14. S. SUZUKI, T. SASAYAMA, M. MIKI, M. OHSUGA, S. TANAKA, S. UENO and N. ICHIKAWA, SAE Paper No. 860408, 1986.
15. S. UENO, N. ICHIKAWA, S. SUZUKI and K. TERAKADO, SAE Paper, No. 860409, 1986.
16. W. C. VASSELL, E. M. LOGOTHETIS and R. E. HETRICK, SAE Paper, No. 841250, 1984.
17. S. SOEJIMA and S. MASE, SAE Paper, No. 850378, 1985.
18. T. SASAYAMA, T. YAMAUCHI, R. BYERS, S. SUZUKI and S. UENO, SAE Paper, No. 910501, 1991.
19. A. D. COLVIN, J. S. RANKIN and K. R. CARDUNER, *Sensors and Actuators* B **12** (1993) 83.
20. S. SUZUKI, T. SASAYAMA, M. MIKI, H. YOKONO, S. IWANAGA and S. UENO, SAE Paper, No. 850379, 1985.
21. K. SAJI, *J. Electrochem. Soc.* **134** (1987) 2430.
22. S. OH and M. MADOU, *Sensors and Actuators* B **13–14** (1992) 581.
23. K. ISHIBASHI, T. KASHIMA and A. ASADA, *ibid.* **13–14** (1993) 41.
24. K. KANEYASU, T. NAKAHARA and T. TAKEUCHI, *ibid.* **13–14** (1993) 34.
25. B. Y. LIAW and W. WEPPNER, *Solid State Ionics* **40/41** (1990) 428.
26. T. TAKEUCHI and I. IGARASHI, in "Chemical Sensor Technology" Vol. 1, edited by T. Seiyama (Elsevier, 1991) p. 79.
27. J. S. HEPBURN, D. A. DOBSON, C. P. HUBBARD, S. O. GULDBERG, E. THANASIU, W. L. WATKINS, B. D. BURNS and H. S. GANDI, SAE Paper No. 842057, 1994.
28. A. H. MEITZLER, SAE Paper No. 800019, 1980.
29. W. B. CLEMMENS, M. A. SABOURIN and T. RAO, SAE Paper No. 900062, 1990.
30. J. W. KOUPAL, M. A. SABOURIN and W. B. CLEMMENS, SAE Paper No. 910561.
31. K. MORIYA and T. SAKO, *Sensors and Actuators* B **73** (2001) 142.
32. W. WEPPNER and H. SCHUBERT, in "Advances in Ceramics," Vol. 24B, edited by S. Somiya, N. Yamamoto and H. Yanagina (The American Ceramic Society, Inc., Westerville, Ohio, 1988) p. 837.
33. E. M. LOGOTHETIS, in "Advances in Ceramics," Vol. 3, edited by A. H. Heuer and L. W. Hobbs (The American Ceramic Society, Inc., Westerville, Ohio, 1981) p. 388.
34. E. ELTINGE, SAE Paper No. 680114, 1968.
35. J. E. ANDERSON and Y. B. GRAVES, *J. Electrochem. Soc.: Electrochem. Sci. and Techn.* **128** (1981) 294.
36. D. R. HAMBURG and M. A. SHULMAN, SAE Paper No. 800826, 1980.
37. J. A. COOK, D. R. HAMBURG, W. J. KAISER and E. M. LOGOTHETIS, SAE Paper No. 830985, 1983.
38. K. SAJI, H. KONDO, T. TAKEUCHI and I. IGARASHI, *J. Electrochem. Soc.: Electrochem. Sci. and Techn.* **135** (1988) 1686.
39. W. J. FLEMING, *J. Electrochem. Soc.* **12** (1977) 21.
40. S. ISHIKAWA, Y. NODA, N. HAYAKAWA, S. KAWAJIRI and H. IIMI, SAE Paper No. 980263, 1998.
41. H.-M. WIEDENMANN, L. RAFF and R. NOACK, SAE Paper No. 840141, 1984.
42. H. NEUMANN, G. HOTZEL and G. LINDEMANN, SAE Paper No. 970459, 1997.
43. S. KIMURA, H. TAKAO, S. AMBE and Y. AKIMUNE, US Patent No. 4347114, (1982).
44. B.-K. KIM, KR 161498 (1999).
45. E. J. DETWILER, R. C. KUISELL and J. V. BONADIES, US Patent No. 6482310 (2002).
46. K. SONE and K. OKAMURA, US Patent no. 4359030 (1982).
47. P. S. BRETT, A. L. NEVILLE, W. H. PRESTON and J. WILLIAMSON, SAE Paper No. 890490, 1989.
48. F. UEDA, S. SUGIYAMA, K. ARIMURA, S. HAMAGUCHI and K. AKIYAMA, SAE Paper No. 940746, 1994.
49. W. C. MASKELL, *J. Phys. E: Sci. Instrum.* **20** (1987) 1156.
50. D. M. HAALAND, *J. Electrochem. Soc.* **127** (1980) 796.
51. T. USUI, A. ASADA, M. NAKAZAWA and H. OSANI, *J. Electrochem. Soc.* **136** (1989) 534.
52. H. DIETZ, *Solid State Ionics* **6** (1982) 175.
53. T. USUI, K. NURI, M. NAKAZAWA and H. OSANI, *Jpn. J. Appl. Phys.* **26** (1987) L2061.
54. E. N. FULLER, P. D. SCHETTLER and J. C. GIDDINGS, *Ind. Eng. Chem.* **58** (1966) 19.
55. E. N. FULLER, K. ENSLEY and J. C. GIDDINGS, *J. Phys. Chem.* **73** (1969) 3679.
56. T. USUI, A. ASADA, M. NAKAZAWA and H. OSANI, *Jpn. J. Appl. Plys.* **28** (1989) L1654.
57. J.-H. LEE, B.-K. KIM and H. KIM, *Solid State Ionics* **86–88** (1996) 1087.
58. T. YAMADA, N. HAYAKAWA, Y. KAMI and T. KAWAL, SAE Paper No. 920234, 1992.

59. H. TANAKA, S. NISHIMURA, S. SUZUKI, M. MIKI, T. HARADA, M. KANAMARU, S. UENO and N. ICHIKAWA, SAE Paper No. 890299, 1989.
60. H.-I. KIM, J.-H. LEE and B.-K. KIM, in Proccedings of The Third IUMRS International Conference in Asia (IUMRS-ICA-'95), Fabrication and Characterization of Advanced Materials, edited by S. W. Kim and S. J. Park (The Materials Society of Korea, 1995).
61. S. OH, *Sensors and Actuators* B **20** (1994) 33.
62. B.-K. KIM, J.-H. LEE and H.-I. KIM, *Solid State Ionics* **86–88** (1996) 1079.
63. H.-I. KIM, B.-K. KIM and K.-Y. LEE, European Patent No. 0856732 (1998).
64. J.-H. LEE, DE 19848578; KR269211 (1999).
65. J.-H. LEE, B.-K. KIM, K.-Y. LEE, H.-I. KIM and K.-W. HAN, *Sensors and Actuators* B **59** (1999) 9.
66. J.-H. LEE, C.-S. KWON, H.-I. KIM and B.-K. KIM, *ibid.* B **35–36** (1996) 278.
67. J.-H. LEE and K.-Y. LEE, US Patent no. 6077409 (2000).